Biophysical Journal Volume 68 April 1995 1231–1245

Dynamic and Elastic Properties of F-Actin: A Normal-Modes Analysis

Daniel ben-Avraham and Monique M. Tirion
Department of Physics, Clarkson University, Potsdam, New York 13699-5820 USA

ABSTRACT We examine the dynamic, elastic, and mechanical consequences of the proposed atomic models of F-actin, using a normal mode analysis. This initial analysis is done in vacuo and assumes that all monomers are rigid and equivalent. Our computation proceeds from the atomic level and, relying on a single fitting parameter, reproduces various experimental results, including persistence lengths, elastic moduli, and contact energies. The computations reveal modes of motion characteristic to all polymers, such as longitudinal pressure waves, torsional waves, and bending, as well as motions unique to F-actin. Motions typical to actin include a "groove-swinging" motion of the two long-pitch helices, as well as an axial slipping motion of the two strands. We prepare snapshots of thermally activated filaments and quantify the accumulation of azimuthal angular "disorder," variations in cross-over lengths, and various other fluctuations. We find that the orientation of a small number of select residues has a surprisingly large effect on the filament flexibility and elasticity characteristics.

INTRODUCTION

Actin, an assembly-triggered ATPase present in all eukaryotic cells, is involved in cell transport, cytoskeletal support, and contractile events. In non-ionic solutions actin exists in a monomeric form called G-actin. In the presence of traces of salt, such as found in vivo, actin monomers polymerize into helical polymers called F-actin. As actin functions only as a polymer, much effort is directed to understanding and characterizing the properties of this filament. Furthermore, recent experiments provide compelling evidence that a large fraction of the sarcomere compliance resides in the thin filaments (Huxley et al., 1994; Wakabayashi et al., 1994), and hence a theoretical derivation of the longitudinal, torsional, and bending stiffness of actin filaments is well warranted.

The sequence, and presumably therefore the structure, of actin has changed little over the course of vertebrate evolution. The sequence similarities of actin found in mammals, birds, amphibians, and fish is over 90% (Doolittle, 1990). Natural selection, in other words, has selected a very particular set of structural characteristics that permits this protein to fulfill its functional roles. A particular structure gives rise to a unique dynamical spectrum: the internal flexibility and mobility characteristics of F-actin are uniquely determined by its intermonomer and intramonomer interactions. To date, however, analyses of the mechanical properties of actin have largely relied on simple "wire" models: actin filaments modeled as homogeneous cylinders. This permits the components of an overly simplified tensor of elasticity to be deduced from experimental data. However, such a macroscopic approach ignores a potentially vast range of motions and flexibilities that result from the particular three-dimensional atomic models of the filament and that are unique to F-actin.

We study the dynamic, elastic, and mechanical consequences of the proposed atomic models of F-actin, using a normal mode analysis (NMA). A NMA is appealing because it is easy to implement, proceeds from the atomic structure of the model, and presents results in terms of simple vibrational mobilities that are readily visualized and understood. The use of normal modes as a reliable analytical tool has been demonstrated by the ability to reproduce crystallographic temperature factors with a finite set of modes; such analyses indicate the extent to which atomic mobilities are a result of intramolecular versus intermolecular, or lattice, vibrations (Diamond, 1990; Kidera and Gō, 1992). Recently Faure and co-workers (1994) analyzed the distinct diffuse x-ray scatter from lysozyme crystals, using molecular dynamics and normal mode analyses. They found that, in vacuo, normal modes reproduce the diffuse scatter patterns more accurately than a molecular dynamics simulation. (They did not attempt the analysis in a solvent environment.)

In this initial analysis of the dynamical spectrum of F-actin, the computation is carried out in vacuo and disregards the internal flexibilities within the actin monomers. Although these restrictions will be relaxed in future work, initial results are encouraging. We reproduce the regular modes of continuum "wire" models (torsion, stretching, and bending), plus the associated coefficients of elasticity. These parameters, in turn, may be used to predict the deformations induced by external torques and forces, such as imposed, perhaps, by myosin. Beyond the "wire" modes, we compute a rich variety of motions that are unique to actin and that depend on the details of the atomic models. In this respect, we find that the analysis is sensitive to the orientation of a few key loops and regions, such as the DNase I-binding loop and the 262–274 "plug."

F-actin structure

The F-actin helix possesses a rise per monomer of 27.5 Å and a rotation angle of $-166.15°$ per monomer around the fila-

Received for publication 25 July 1994 and in final form 31 October 1994.

Address reprint requests to Dr. Monique M. Tirion, Department of Physics, Clarkson University, Box 5820, Potsdam, NY 13699-5820. Tel.: 315-268-2375; FAX: 315-268-6670; E-mail: tirion@craft.camp.clarkson.edu.

© 1995 by the Biophysical Society

0006-3495/95/04/1231/15 $2.00

ment axis (assuming a 13/6-actin helix with a repeat of 35.75 nm). Thus the *genetic* helix is left-handed, but, because the rotation per monomer is close to 180°, the structure has the appearance of two right-handed long-pitch helices that slowly twist around each other.

The crystal structure of rabbit skeletal G-actin complexed with bovine pancreatic DNase I is known (Kabsch et al., 1990) and is closely similar to the structures of monomeric actin complexed with gelsolin (McLaughlin et al., 1993) and profilin (Schutt et al., 1994). Atomic models of the F-actin filament have been developed (Holmes et al., 1990; Lorenz et al., 1993; Tirion et al., 1995). Structural data of F-actin obtained by x-ray fiber diffraction from aligned gels (Popp et al., 1987), extend to ~7-Å resolution; hence a unique model of the actin filament does not exist. Indeed, recent experiments suggest that actin may exist in different configurations, depending upon the identity of the bound cation and state of the nucleotide, for example (Orlova and Egelman, 1992, 1993).

The original model of F-actin, developed using four adjustable parameters, assumed that the structure of the monomer does not change upon incorporation into the filament (Holmes et al., 1990). Subsequent work has shown that minor modifications of the initial model significantly improve the R factor, the fit of the computed diffraction pattern to the observed x-ray fiber diffraction data. Refinements and biochemical data indicate that the nucleotide binding cleft closes upon incorporation into the filament (Lorenz et al., 1993; Tirion et al., 1995; Miki and Kouyama, 1994). The DNase I binding loop in subdomain 2 and the COOH-terminal region seem to be rather flexible and are not uniquely oriented by the refinements.

Holmes et al. have hypothesized that a hydrophobic loop or "plug" straddling subdomains 3 and 4 extends into a hydrophobic hole in the opposing strand to stabilize the F-actin structure (Holmes et al., 1990). This assertion is not inconsistent with the fiber diffraction data, but it is not proven by site-directed mutagenesis experiments (Chen et al., 1993). We do not favor any particular model of F-actin, but rather report on the mechanical, dynamical, and elastic consequences of each proposed model. Our analyses of different models indicate that the orientations of a few loops have dramatic effects on the flexibilities of F-actin.

Normal modes

An NMA describes small-amplitude harmonic oscillations about a single, equilibrium configuration. It requires (a) defining the degrees of freedom of the assembly and (b) determining a potential energy that is quadratic in these degrees of freedom. In practice, the potential energy is minimized and a quadratic form is obtained through a Taylor expansion about the minimum. In this study, we treat the filament as being built up from *rigid* actin monomers and allow each monomer six independent degrees of freedom (three translations and three rotations). For the potential energy, which describes the intermonomer "bonds," we first identify all atom pairs that are within a certain cutoff distance between neighboring monomers. A harmonic energy function is then defined that is a function of the distances of separation; each interaction is treated equivalently.

The atomic model of F-actin is derived from 7-Å fiber diffraction data, and hence the orientation of side chains, especially at the surface, are not uniquely resolved. However, the surface residues determine the noncovalent intermonomer interactions, or "bonds". Our formulation of the potential energy broadly reflects the surface areas and orientations of the bonds, and does not require specification of the exact nature of the electrostatic interactions, which, at this point, given the limited information on the surface-residue orientations and role of solvent in forming the intermonomer bonds, would be unjustified. (As the details of the atomic model of F-actin improve, this formulation can be adjusted). In addition, the energy function that we use is already minimal at the atomic configuration of the proposed models. This allows us to proceed from the published atomic configurations without initial modifications of the structures.

Macromolecular assemblies, because of their size and complexity, are difficult to characterize, both computationally and physically. Here we present an initial attempt to compute the mechanical, dynamical, and elastic consequences of a proposed macromolecular assembly, based on an atomic, structure-based analysis. In restricting ourselves to rigid monomers, relevant features of actin mobility will undoubtedly be ignored, and the usefulness of the computation must be judged in terms of how successfully certain properties, such as bending and stretching rigidities, are reproduced. By further refinement of the model, such as inclusion of internal degrees of freedom within the monomers, it may be possible to better understand which filament characteristics are a consequence of which physical properties. Similarly, the restriction of our analysis to vacuum, ignoring hydrodynamic effects, will affect the time scales of the computed motion (motion is overdamped) and possibly the nature of some modes. However, bearing in mind that both crystallographic temperature factors as well as diffuse x-ray scatter is well reproduced with normal mode analyses, it seems that the solvent does not dramatically alter the appearance, or eigenvectors, of the low-energy modes (which contribute most to the observed temperature factors and diffuse scatter). Among these modes, we identify, for example, a groove-angle swinging motion of the two long-pitch helices, as well as an axial slipping motion between the long-pitch helices.

In the next section (Method), we show in detail how the general theory of normal modes can be applied to F-actin. It should be borne in mind that the ideas presented here are quite general and can be adapted to other periodic structures with only minor modifications. In subsequent sections, we describe and discuss our findings for F-actin.

METHODS

We analyze the normal modes of a fiber using standard techniques of Classical Mechanics (Goldstein, 1980; Marion, 1970; Levitt et al., 1985). We start by selecting a convenient set of generalized coordinates, $\{q\}$.

Dynamic variables

Because the fiber is made up from monomers, it is natural to index the generalized coordinates with two indices, $q_{n\nu}$. The first index, n, denotes the monomer in question, and the second index, ν, indicates a specific degree of freedom available to monomer n.

A minimal set of a monomer's degrees of freedom should include three-dimensional translations and rotations of the monomer as a whole. Employing such a minimal set amounts to the assumption that the G-actin monomers are rigid. The internal flexibility of the monomers can be taken into account in various ways. One straightforward, appealing approach is to use the slowest normal modes of motion found for G-actin (Tirion and ben-Avraham, 1993). In this fashion, F-actin is understood as a periodic chain of fanciful springs, each of which may oscillate as described by the slowest modes of G-actin. In this paper, however, we report preliminary results (in which the degrees of freedom per monomer include only overall translations and rotations. The internal flexibility of G-actin is taken into account, loosely, through the adjusting of the phenomenological potential energy of contact between monomers.

We describe the motion of monomer n with respect to *its own* set of Cartesian coordinates. The set of coordinates for the $(n + 1)$-th monomer is obtained from that of the nth monomer:

$$\begin{pmatrix} x_{n+1} \\ y_{n+1} \\ z_{n+1} \end{pmatrix} = \mathbf{U}\begin{pmatrix} x_n \\ y_n \\ z_n \end{pmatrix} + \mathbf{Z}, \tag{1}$$

where $\mathbf{U}$ is the rotation matrix used to construct the filament (Holmes et al., 1990) and $Z = 27.5$ Å is the rise per monomer.

The six (minimal) degrees of freedom of monomer n are chosen to be

$$\mathbf{q}_n \equiv \begin{pmatrix} q_{n1} \\ q_{n2} \\ q_{n3} \\ q_{n4} \\ q_{n5} \\ q_{n6} \end{pmatrix} = \begin{pmatrix} x_n \\ y_n \\ z_n \\ \alpha_n \\ \beta_n \\ \gamma_n \end{pmatrix}. \tag{2}$$

Here q_{n1}, q_{n2}, and q_{n3} denote parallel translation $\Delta\mathbf{r}_n = (x_n, y_n, z_n)$ and q_{n4}, q_{n5}, and q_{n6} represent axial rotations of angular magnitude α_n, β_n, and γ_n around the x_n, y_n, and z_n axes, respectively, about the center of mass of monomer n. The various values of q are defined as changes from the equilibrium configuration, so that at equilibrium $q_{n\nu} = 0$.

The normal modes of the fiber will reflect its periodic structure. Thus, without loss of generality, we may write

$$q_{n\nu} = q_\nu e^{in\phi}, \tag{3}$$

where ϕ is the phase lag in the motion between adjacent monomers.

General theory of normal modes

Given the set of generalized coordinates, the potential energy, E_p, can be approximated by a quadratic expansion:

$$E_p = \frac{1}{2}\sum_{n\nu,m\mu} q_{n\nu}F_{n\nu,m\mu}q_{m\mu} = \frac{1}{2}\mathbf{q}^\dagger\mathbf{F}\mathbf{q}, \tag{4}$$

where the dagger represents the transpose operation and the $\mathbf{F}$ elements are

$$F_{n\nu,m\mu} = \left(\frac{\partial^2 E_p}{\partial q_{n\nu}\,\partial q_{m\mu}}\right)_{\mathbf{q}=0}. \tag{5}$$

The kinetic energy is written as a quadratic polynomial of the generalized velocities, $q_{n\nu}$ (the dot denotes differentiation with respect to time):

$$E_k = \frac{1}{2}\dot{\mathbf{q}}^\dagger\mathbf{H}\dot{\mathbf{q}}, \tag{6}$$

with

$$H_{n\nu,m\mu} = \sum_l m_l \frac{\partial\mathbf{r}_l}{\partial q_{n\nu}}\cdot\frac{\partial\mathbf{r}_l}{\partial q_{m\mu}}, \tag{7}$$

and the summation runs over all atoms l of the filament.

The modes are obtained from the solution to Lagrange's equation:

$$\frac{d}{dt}\left(\frac{\partial\mathcal{L}}{\partial\dot{q}_{n\nu}}\right) = \frac{\partial\mathcal{L}}{\partial q_{n\nu}}, \tag{8}$$

where $\mathcal{L}$ is the Lagrangian $\mathcal{L} = E_k - E_p$.

Energy of contact between monomers

The potential energy of contact between adjacent monomers in the fiber is crucial to the derivation of the normal modes. For rigid monomers, as assumed in this work, the contact between monomers is the only source of potential energy. Because of the symmetry of the actin filament, each G-actin monomer makes contact with four other monomers. There are two types of contact: contact between monomers n and $n + 1$ and contact between monomers n and $n + 2$. These have been called the "diagonal bond" and the "longitudinal bond", respectively (Erickson, 1989). Thus, denoting the contact potential energy between monomers n and m as $E_{n,m}$, we can express the total potential energy as

$$E_p = \sum_n (E_{n,n+1} + E_{n,n+2}). \tag{9}$$

The binding energy between monomers is due to noncovalent "bonds": both nonpolar dispersive and hydrophobic-exclusion interactions, as well as polar and ionic forces. The strength of these "bonds" is a sensitive function of the distance of separation of the interacting atom pairs and will of course be proportional to the total contact area between consecutive monomers. Lacking detailed knowledge of the exact nature of all intermonomer interactions, we opt to model the energy function as a simple pairwise interaction between atom a in monomer n and atom b in monomer m:

$$E(\mathbf{r}_{na}, \mathbf{r}_{mb}) = (C/2)(|\mathbf{r}_{na,mb}| - |\mathbf{r}^0_{na,mb}|)^2. \tag{10}$$

Here $\mathbf{r}_{na,mb} = \mathbf{r}_{na} - \mathbf{r}_{mb}$ denotes the vector connecting the two atoms in question and the zero superscript indicates the equilibrium (initial) configuration. This pairwise potential is spherically symmetric and has a minimum at the equilibrium configuration. Expanding to second order about $\mathbf{r}^0_{na,mb}$, we obtain the simpler form

$$E(\mathbf{r}_{na}, \mathbf{r}_{mb}) = \frac{C}{2}\left(\frac{\mathbf{r}^0_{na,mb}\cdot\Delta\mathbf{r}_{na,mb}}{|\mathbf{r}^0_{na,mb}|}\right)^2, \tag{11}$$

where $\Delta\mathbf{r} \equiv \mathbf{r} - \mathbf{r}^0$.

The strength of the potential, C, is a phenomenological constant that is assumed to be the same for all interacting pairs. The potential energy of contact between monomers n and m is then given by

$$E_{n,m} = \sum_{\{a,b\}} E(\mathbf{r}_{na}, \mathbf{r}_{mb}), \tag{12}$$

where the sum runs over all pairs of atoms $\{a, b\}$ whose distance does not exceed their combined Van der Waals radii plus a cutoff distance d; $|\mathbf{r}^0_{na,mb}| \leq r_a^{VW} + r_b^{VW} + d$. We set $d = 2$ Å.

Equations 9, 11, and 12 specify the total potential energy of the filament. This potential has been selected for its many advantages. By virtue of Eq. 11 the potential is minimal at the equilibrium configuration. This dispenses with the lengthy and costly process of minimization. The simple form of the potential also facilitates the derivation of the F elements (Eq. 5). Finally, the assumed potential introduces only one phenomenological parameter, C, so that the model's predictions will not be due to excessive parameter fitting.

F-actin models considered

Ultimately, the potential energy depends on the atomic model of the actin filament, for it is the atomic model that determines which, and how many, atom pairs interact. We will consider four models, which are very similar except in the orientation of a few loops and regions, especially the DNase I binding loop and the 262–274 hydrophobic "plug." We will first consider the original model of Holmes et al. (1990) (H model), derived from x-ray fiber diffraction data, using the exact crystallographic coordinates of G-actin as a model for the monomer. We also consider this model, but with the hydrophobic 262–274 "plug" straddling subdomains 3 and 4 rebuilt (P model). This loop is hypothesized to stabilize the F-actin structure when it is reoriented to interact with a hydrophobic region of two neighboring monomers in the opposing strand (Holmes et al., 1990). The R factor, to ~8-Å resolution, is approximately the same (0.19) for these two models.

Also, we consider the refined models of Tirion et al. (1995) (T model) and Lorenz et al. (1993) (L model). The T model of F-actin, developed by refining the H model (i.e., the crystal coordinates) using a normal modes algorithm (Tirion et al., 1995), shifted domains without altering the intradomain structure significantly. The rms deviation of the main-chain atoms of the large domains of the T and H models is 1.4 Å, whereas the equivalent r.m.s. fit of the small domains is 0.9 Å. The normal mode refinement closed the nucleotide binding cleft, by shifting the small domain, propeller-style. The DNase I-binding loop has narrowed, twisting upward. In the helix, this refinement has situated these residues in the cleft between subdomains 1 and 3 of the next monomer in the long-pitch helix. Also, the hydrophobic "plug" was not rebuilt for this refinement, and although this loop has shifted laterally, it has not extended toward the opposing strand as in the P-model.

The L-model of actin (Lorenz et al., 1993) was obtained by refining the P model, using a "directed mutation" algorithm. The rms deviation of the mainchain atoms of one monomer of the L model and the H model (i.e., the crystal coordinates) is 2.4 Å. The L model allows the largest structural deviations from the crystal coordinates and achieves the lowest R factor (below 0.05). The refinement incorporates the rebuilt 262–274 "plug" as well as a manual rebuilt of the DNase I binding loop. This latter region (approximately residues 38–52) folds back onto subdomain 2 in a manner such as to close the nucleotide-binding cleft. In the filament, this results in increased interaction of subdomain 2 with subdomain 3 in the next monomer in the long-pitch helix. There are no longitudinal contacts between subdomain 2 and subdomain 1 of a neighboring long-pitch monomer, unlike the T-model. The dynamical and mechanical consequences of these alternate locations of the DNase I binding regions as well as the 262–274 "plug" are interesting to monitor. A comparison of results is presented in a later section.

General form of solutions

Consider, for simplicity, an infinite filament. This avoids the issue of boundary conditions, which we postpone momentarily. Because of our choice of dynamic variables, which describe the motion of each monomer with respect to its own system of coordinates, and because of the symmetry of the filament, the matrices **F** and **H** assume the simple block form

$$\mathbf{F} = \begin{pmatrix} \ddots & & & & & & \\ \mathbf{g}^\dagger & \mathbf{f}^\dagger & \mathbf{d} & \mathbf{f} & \mathbf{g} & & \\ & \mathbf{g}^\dagger & \mathbf{f}^\dagger & \mathbf{d} & \mathbf{f} & \mathbf{g} & \\ & & \mathbf{g}^\dagger & \mathbf{f}^\dagger & \mathbf{d} & \mathbf{f} & \mathbf{g} \\ & & & & & \ddots & \end{pmatrix},$$

$$\mathbf{H} = \begin{pmatrix} \ddots & & & & \\ & \mathbf{h} & & & \\ & & \mathbf{h} & & \\ & & & \mathbf{h} & \\ & & & & \ddots \end{pmatrix}, \tag{13}$$

where **d**, **f**, **g**, and **h** are (6 × 6) matrices (for their explicit elements, see Appendix A).

In terms of the spatially periodic form of q of Eq. 3, Lagrange's equation becomes

$$-\bar{\mathbf{f}}\mathbf{q} = \mathbf{h}\ddot{\mathbf{q}}. \tag{14}$$

Here **q** denotes the six-dimensional vector q_ν, and

$$\bar{\mathbf{f}} = \mathbf{g}^\dagger e^{-2i\phi} + \mathbf{f}^\dagger e^{-i\phi} + \mathbf{d} + \mathbf{f}e^{i\phi} + \mathbf{g}e^{2i\phi} \tag{15}$$

is a Hermitian (6 × 6) matrix that depends on the spatial phase lag, ϕ.

To obtain the normal modes, we seek solutions periodic in time, of the form

$$q_\nu = \sum_\mu A_{\nu\mu}(\phi)\alpha_\mu(\phi)\cos(\omega_\mu(\phi)t + \delta_\mu(\phi)), \tag{16}$$

where α_μ and δ_μ are arbitrary constants. Using this in Eq. 14, one gets the normal modes equation

$$\bar{\mathbf{f}}\mathbf{A} = \mathbf{\Lambda}\mathbf{h}\mathbf{A}. \tag{17}$$

The eigenfrequencies are given by the elements of the diagonal matrix $\mathbf{\Lambda}$, $\omega_\nu(\phi)^2 = \Lambda_{\nu\nu}$, and the eigenvectors are the columns of the matrix **A**. Although the elements of the **A** matrix are not necessarily real, a general motion of the filament is real and can be expressed in terms of the normal modes:

$$q_{n\nu} = \sum_\phi \sum_\mu |A_{\nu\mu}(\phi)|\,\alpha_\mu(\phi)\cos(n\phi + \theta_{\nu\mu}(\phi) + \delta'_\nu(\phi)) \times \cos(\omega_\mu(\phi)t + \delta_\mu(\phi)). \tag{18}$$

Here $\theta_{\nu\mu}(\phi) = \arg(A_{\nu\mu}(\phi))$ and δ' is an arbitrary constant. The constants α, δ, and δ' are determined from the initial state of the fiber at time $t = 0$. In the case of filaments in a heat bath the α amplitudes assume a characteristic value that is temperature dependent. These are derived in Appendix B, where we analyze the thermodynamics of the filament.

Equation 17 fixes **A** only up to a normalization constant. If we require the normalization condition

$$\mathbf{A}^\dagger\mathbf{h}\mathbf{A} = \mathbf{I}, \tag{19}$$

the potential and the kinetic energy can then be written as a diagonal quadratic expression in $Q_\mu(\phi) \equiv \alpha_\mu(\phi)\cos(\omega_\mu(\phi)t + \delta_\mu(\phi))$ and $\dot{Q}_\mu(\phi)$. That is, the $Q_\mu(\phi)$ are the *normal modes* of motion that diagonalize the Hamiltonian, $\mathcal{H} = E_p + E_k$.

Boundary conditions

We now turn to the problem of boundary conditions. For a strictly infinite filament the boundary conditions are undefined, and one gets a continuous

spectrum of normal modes. In this case, the spatial phase lags ϕ form a continuum, $0 \le \phi \le \pi$, and the outer sum in Eq. 18 should really be replaced by an integral. In the more physical case of a finite filament consisting of N monomers, the boundary conditions determine a discrete set of accessible wave phases ϕ: the ϕ's assume N possible values that are nearly equally spaced ($\Delta\phi = \pi/N$).

The conditions at the edges of the filament—whether these are fixed or constrained in any fashion or allowed to move freely—determine the actual values of ϕ. For short wavelengths, the kinetics of the fiber is unaffected by the specific boundary conditions. Specific boundary conditions need be taken into account only for those modes of motion involving the longest coherence lengths, of the order of the length of the entire filament.

Quenched thermal motion

In principle, one can compute any thermal average from the elementary pair correlations developed in Appendix B. In practice, however, several of the fluctuations of interest involve functions of many coordinate variables. The decomposition of such multivariable expressions into pair averages is tedious and cumbersome. A simple way to overcome this difficulty is to perform statistical averages on a random ensemble of thermally excited fibers. In the following, we show how to develop snapshots of F-actin, trapped in typical configurations of thermal agitation.

The basic idea is to compute the coordinates of the fiber at some arbitrary time, $t = t_0$, according to Eq. 18, with the characteristic α's at temperature T (Appendix B). Recall that the phases δ' and δ depend on initial conditions. We therefore pick these phases at random, from a homogeneous distribution over the interval $[0, 2\pi]$. Having made these assumptions, there is nothing particular about the actual value of the initial time, t_0, and we may choose $t_0 = 0$, for simplicity. We then have

$$q_{j\mu} = \sum_{\phi} \sum_{\sigma} |A_{\mu\sigma}(\phi)|\, \alpha_\sigma(\phi)\cos(j\phi + \theta_{\mu\sigma}(\phi) + \delta'_\sigma(\phi))\cos(\delta_\sigma(\phi)). \qquad (20)$$

In Fig. 1 we show schematically one such configuration rotated through incremental angles from 0° to 180°. The overall bending of the fiber, as well as other local deformations, can be appreciated from this plot. In Fig. 2 we plot 10 such different configurations of quenched thermal agitation. Each of these configurations has been produced with a different choice of the random phases δ' and δ in Eq. 20. Statistics of interest, such as the bending curvature of fibers or the distribution of the number of monomers per repeat (the crossover length), can be performed directly on the computer-generated ensemble, in much the same way as done with EM data.

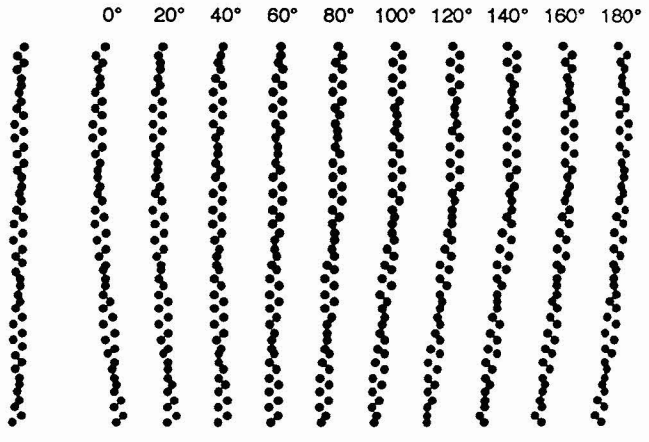

FIGURE 1 Configuration of simulated thermal disorder in F-actin. The 40-monomers filament is shown rotated through incremental angles of 20°. An unperturbed filament is shown for comparison (left).

RESULTS

We now present our results in terms of the original H model of Holmes et al. (1990). In a later section we will make comparisons between the results obtained using different models of F-actin.

Computation of the potential strength C

To obtain numerical predictions about F-actin, we need to estimate the strength of the potential C (Eq. 11). Any experimental measure can be used for such an estimate. The idea is to fit C so that the model's prediction matches the experiment. We choose to base our computation on measurements of the stretching elasticity of F-actin (Kojima et al., 1994; Huxley et al., 1994; and Wakabayashi et al., 1994). We prefer this experimental measure because the elastic constant has a minimal dependence on the solvent, which is neglected in our analysis. The experiment for measuring the elastic strength of the filament is also appealing in its simplicity; it is basically done by applying a stretching force to the ends of a filament, or a bundle of filaments, and recording the elongation.

Suppose that a filament of length $L = NZ$ ($Z = 27.5$ Å is the rise per monomer) is stretched by an amount Δz. The distance between two consecutive monomers, i and $i + 1$, is then incremented by $\Delta z/N$, and that between monomers i and $i + 2$ is stretched by $2\Delta z/N$. According to the energy function of Eqs. 9–12, the potential energy of the fiber grows by

$$\Delta E_p = \frac{NC}{2}\left[\sum_{\{a,b\}}\left(\frac{\mathbf{r}^0_{ia,(i+1)b}\cdot\mathbf{k}}{|\mathbf{r}^0_{ia,(i+1)b}|}\right)^2 + 4\sum_{\{c,d\}}\left(\frac{\mathbf{r}^0_{ic,(i+2)d}\cdot\mathbf{k}}{|\mathbf{r}^0_{ic,(i+2)d}|}\right)^2\right]\left(\frac{\Delta z}{N}\right)^2, \qquad (21)$$

where k is a unit vector in the z direction. This can be rewritten in terms of elements of the F matrix as (see Appendix A):

$$\Delta E_p = \frac{C}{2N}(f_{33} + 4g_{33})(\Delta z)^2. \qquad (22)$$

On the other hand, if the filament has an elastic constant K, then its potential energy from stretching is simply $\Delta E_p = K(\Delta z)^2/2$. Comparing this with Eq. 22 we obtain

$$C = \frac{NK}{f_{33} + 4g_{33}}. \qquad (23)$$

Kojima et al. (1994) find for 1-μm actin filaments, polymerized with phalloidin, that $K = 43.9 \pm 4.0$ pN/nm. Using this figure and Eq. 23, we compute $C = 0.0149$ kcal/Å^{2}mol (for the H model of F-actin). We derive a similar value of K, and hence of C, using the diffraction data from relaxed and stretched myofilaments of Sosa et al. (1994), Huxley et al. (1994), and Wakabayashi et al. (1994). We emphasize that the value of C per se has little microscopic physical

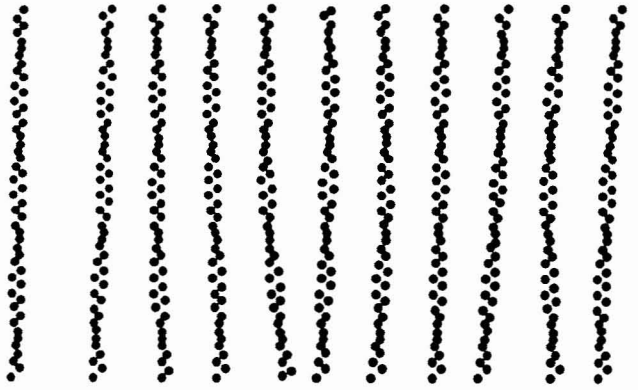

FIGURE 2 A sample of 10 different configurations of F-actin representing thermal disorder. An unperturbed filament is shown for comparison (left).

meaning. It should be regarded as a purely phenomenological parameter.

Dispersion relation and normal modes

We now use the theory outlined in the previous sections to compute the eigenfrequencies and the normal modes of the filament. After a computation of the d, f, g, and h matrices (Appendix A) we select a wave phase $0 \leq \phi \leq \pi$ (or, alternatively, a wave number $k = \phi/Z$) and compute the $\tilde{f}$ matrix of Eq. 15. We then use standard diagonalization algorithms, provided by the mathematical package MATLAB (The Math Works, Inc., S. Natick, MA), to obtain the six eigenfrequencies $\omega_\nu(\phi)$ and their corresponding eigenvectors. Repeating this procedure for different values of ϕ yields the dispersion relation (ω as a function of ϕ, or k) shown in Fig. 3.

The six branches in the dispersion relation plot correspond to the six degrees of freedom that we have assigned to each monomer. A point $\omega_\nu(\phi)$ in this plot represents a certain mode of oscillation at frequency ω. Consecutive monomers perform the same motion, but with a phase lag ϕ. The specific motion of the mode at this point is represented by its eigenvector $A_{\mu\nu}$, which provides the relative amplitude of motion of each of the monomer's degrees of freedom. Thus, for example, for $\phi = 0$ ($k = 0$) all monomers move coherently in phase. If ϕ is merely close to zero, monomers move *almost* in phase. If the motion is along the z axis, the result is a longitudinal pressure wave, or a sound wave. As $\phi \to 0$, the energy involved in stretching is increasingly smaller, so that the frequency also tends to zero (as can be inferred from Eq. B1 of Appendix B). Indeed, our computations reveal the existence of such modes—they are indicated in Fig. 3 by curve *a*.

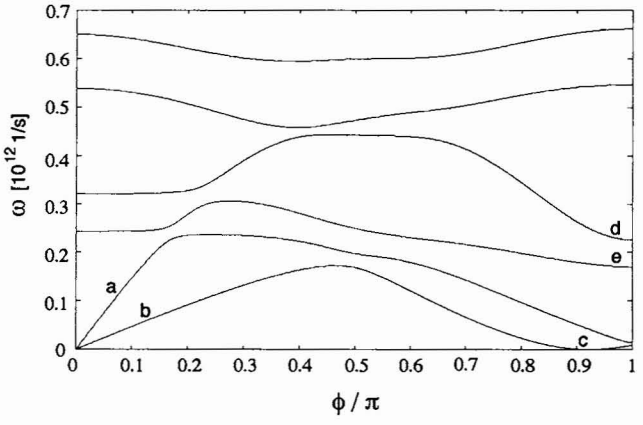

FIGURE 3 Dispersion relations. Shown are the frequencies ω as a function of the wave phase ϕ/π. The six branches correspond to the six degrees of freedom of each G-actin monomer. The labels indicate (*a*) longitudinal modes, (*b*) torsional modes, (*c*) bending modes, (*d*) axial slipping, and (*e*) groove-angle swinging.

Wire modes

The longitudinal pressure waves can be inferred from the simple-minded "wire" model. Regarding the filament as a uniform elastic cylinder with constant K, length L, and longitudinal density M/Z (M is the mass of a monomer), one has $v_{long} = (KLZ/M)^{1/2}$. Using the numbers from the experiment of Kojima et al. (1994) for L and K, we obtain $v = 1313$ m/s. On the other hand, the group velocity of the waves is computed from the dispersion relation: $v_{long} = d\omega/dk = 1310$ m/s (i.e., the slope of branch *a* near the origin). This confirms the correctness of our derivation of C (Eq. 23), as well as the diagonalization protocol.

In addition to the stretching modes near $\phi = 0$, there is yet another kind of acoustic, "wire" mode. Suppose that a monomer rotates around the fiber axis. If the phase $\phi \to 0$, then all other monomers will rotate through the same angle in tandem, resulting in a spinning of the whole filament about its axis. For ϕ slightly greater than zero, we obtain a torsional wave. Again, the energy involved tends to zero (and so does the frequency) as ϕ approaches zero. As expected, we do find such a branch of modes (curve *b* in Fig. 3). From the slope of the plot, we find that torsional waves propagate with $v_{tors} = 410$ m/s. Notice that the group velocity for the torsional motion is smaller than that of the longitudinal pressure wave. This is true for elastic materials in general, regardless of their composition.

When the phase $\phi \approx \phi_0 = 166.15°$, i.e., similar to the angle of rotation between subsequent monomers, another kind of interesting motion occurs. In this case, if a monomer moves in a direction perpendicular to the filament axis, the mismatch in phase between consecutive monomers exactly compensates for the different orientations of their local coordinate systems (see Dynamic variables in the Methods section) and the net result is a transverse motion of the fiber as a whole. Thus, around ϕ_0 we observe transverse oscillations or bending of the fiber (these are indicated in Fig. 3 by curve C). The wavelengths of such oscillations are

$$\lambda_{bending} = \frac{2\pi}{\phi - \phi_0} Z. \qquad (24)$$

Obviously, as $\phi \to \phi_0$ the bending energy approaches zero and so does ω. However, instead of a linear dispersion as for the acoustic waves discussed above, we now have $\omega(\phi) \propto (\phi - \phi_0)^2 \propto (k - k_0)^2$. This seemingly strange behavior is actually normal and can be derived, again, from the simple-minded "wire" model. It will be discussed further in relation to the fiber's flexibility.

Notice that very few modes of motion can be analyzed in terms of a "wire" model. In fact, we have identified all of them (stretching, torsion, and bending). These modes are typical of homogeneous wires of constant cross section and are insensitive to the particular atomic models of the filament. All other modes, the vast majority, are specific to F-actin and are sensitive to the detailed, atomic structure. We will discuss two of these modes. The remaining actin-specific modes, harder to describe, are best understood when visualized with computer animations.

Modes typical of F-actin

Consider now a mode of motion with $\phi = \pi$, at the other edge of the spectrum. This means that consecutive monomers move in an exactly opposite phase. However, every second monomer moves in perfect synchrony with the original one. For example, all the monomers in one strand of the filament may move upward along the positive z direction, while those on the opposing strand would move coherently downward! Obviously, this kind of "axial slipping" motion cannot be predicted on the basis of a "wire" model that does not differentiate between the strands. It is specific to the filament, and we expect it to depend on the atomic model of F-actin, in particular on the orientation of the hydrophobic "plug." Inspection of the modes near $\phi = \pi$ indeed reveals axial slipping motion (curve *d* in Fig. 3).

Another mode at $\phi \approx \pi$ arises when monomers spin around their z axes (*e* in Fig. 3): the two strands spin coherently, in an opposite sense to each other, resulting in a swinging of the groove angle between the strands. Notice that the frequency, ω, of the groove-angle swinging motion is smaller than that of the axial slipping motion. This makes sense if one could model the contact between the two strands as a homogeneous continuous sheet of material. It is usually easier to flex such a sheet, as required by the groove-angle swinging motion, than to shear it, as required by axial slipping. To gain more insight into these motions we need to consider the full atomic model of F-actin (indeed, the results depend strongly on the particular model!).

Interestingly, the last two modes of motion have the wavelength $\lambda = (2\pi/\phi)Z = 2Z$, i.e., the shortest possible. However, one can identify an infinite coherence length (the motion of monomers within each strand is perfectly in phase). Thus, the concept of wavelength is counter-intuitive in this case, as it disagrees so strongly with the coherence length. For this reason we prefer the phase lag between monomers, ϕ, over the more traditional wavelength, or wave number, k.

Also note from Fig. 3 that the fastest oscillations of the fiber are at $\omega = 0.66 \times 10^{12}\ s^{-1}$, corresponding to a period of 9.5 ps. The fastest oscillations of the fiber involve wavelengths of the order of a single monomer; thus one expects that their period would roughly match that of the *slowest* internal oscillations of the monomer (which involve the same length scale). Indeed, we previously found that the slowest period of G-actin is ~17 psec (Tirion and ben-Avraham, 1993), confirming this expectation. Inasmuch as the shortest period of F-actin is proportional to $C^{-1/2}$, this result yields further support to our estimate of C.

Finally, another interesting prediction arising from the dispersion relation of Fig. 3 is a narrow gap of frequencies, from $\omega = 0.44$ to $\omega = 0.46 \times 10^{12}\ s^{-1}$ and from 0.55 to $0.60 \times 10^{12}\ s^{-1}$, in which there exist no vibrational modes. Such gaps are common in the spectra of phonons in solids. It remains to be seen whether these will persist once we include the internal degrees of freedom of the monomers and the effects of the solvent in our computations.

Contact energy between monomers

We can use the spectrum of computed frequencies for the evaluation of various thermodynamic potentials, as shown in Appendix B. For example, we have used Eq. B4 to compute the Gibbs energy per monomer, $\Delta G/N$, at room temperature ($T = 300$ K). This provides us with an upper bound for the Gibbs energy of contact of the diagonal and the longitudinal bonds. $\Delta G/N$ is an overestimate of the contact energy, because vibrations of the fiber include, in addition to the stretching and bending of the contact bonds between monomers, internal elastic energy of the monomers themselves (in our case these internal degrees of freedom influence the value of C). We find $\Delta G/N = 18.4$ kcal/mol. This is in good agreement with the estimates of Erickson (1989), that the combined energies of the diagonal and the longitudinal bonds are smaller than 17 kcal/mol.

Flexibility of F-actin

From the dispersion relations, in particular from the "wire" modes, we can learn about the (macroscopic) elastic coefficients of F-actin. Consider the acoustic pressure waves (branch *a* in Fig. 3). Their speed of propagation is related to the Young's modulus of the fiber, E, through

$$v_{\text{long}} = (E/\rho)^{1/2}, \tag{25}$$

where ρ is the density of F-actin. Thus, knowledge of v_{long} enables us, in principle, to compute the Young's modulus. However, the cross section of F-actin, S, is variable and hence is ill-defined. Using $\rho = M/SZ = \mu/S$

($\mu = M/Z$ is the density per unit length and is less ambiguous than ρ) we obtain the Young's modulus per inverse unit area:

$$ES = \mu v_{long}^2. \tag{26}$$

With the value of $v_{long} = 1310$ m/s, found above for the H model, we get $ES = 4.4 \times 10^{-8}$ N. To obtain an actual value for the Young's modulus, we must estimate the cross-sectional area, S. Simply assuming that F-actin has a uniform circular cross section, with a radius equal to the filament's radius of gyration ($R = 24.1$ Å for the H model), we obtain $E = 2.4 \times 10^9$ N/m^2. This compares very nicely with values for wool, silk, and collagen. Hatta and co-workers (1988) estimate the longitudinal stiffness of resting muscle at 20°C at $E = 2.48 \times 10^9$ N/m^2, as measured with ultrasound, in close agreement with our current derivation.

Consider next the acoustic torsional modes (branch *b* in Fig. 3). Their speed of propagation is related to the torsional rigidity of the filament, ζ, and to the moment of inertia per unit length, I, via

$$v_{tors} = (\zeta/I)^{1/2}. \tag{27}$$

The torsional rigidity is a measure of the resistance of the filament to an external twisting torque. If a torque τ is applied to the filament it results in an angular twist per unit length, ∂_χ/∂_z:

$$\tau = \zeta \frac{\partial \chi}{\partial z}. \tag{28}$$

(Here the angle χ is understood to be measured in radians.) Using $v_{tors} = 410$ m/s in Eq. 27, we get $\zeta = 2.6 \times 10^{-17}$ dyn cm^2.

Finally, we can learn about the flexural rigidity of F-actin from its bending modes (branch *c* in Fig. 3). The coefficient of flexural rigidity, ξ, relates the local curvature of the filament to a local bending moment, M:

$$M = \xi \frac{\partial^2 x}{\partial z^2} \tag{29}$$

(x is the transverse deflection of the axis). Suppose that a filament of length L is clamped at one end and a force F, perpendicular to the filament, is applied to the other end. The deflection of that end would be

$$x = \frac{1}{3} \frac{FL^3}{\xi}. \tag{30}$$

The flexural rigidity can be computed from the dispersion relation of the bending modes:

$$\omega = \left(\frac{\xi}{\mu}\right)^{1/2} (k - k_0)^2. \tag{31}$$

This is, in fact, the "strange" behavior of the bending modes mentioned in the previous section. It arises from consideration of the wave equation of transverse modes for the "wire" model. This equation has a fourth-order spatial derivative, instead of the usual second-order derivative, and is well known within the theory of elasticity of thin rods (see, for example, Landau and Lifshitz, 1959). It is indeed very satisfying that our independent microscopic computations confirm this phenomenological relation. Fitting Eq. 31 to the dispersion relation computed for the bending modes, we find $\xi = 4.3 \times 10^{-17}$ dyn cm^2.

An interesting consequence of the dispersion relation of Eq. 31 is that the velocity of propagation of the transverse bending waves is

$$v_{bend} = 2\left(\frac{\xi}{\mu}\right)^{1/2} (k - k_0). \tag{32}$$

That is, v_{bend} vanishes inversely proportionally to the wavelength (or to the length of the filament, for the longest wavelength). This apparent paradox is resolved when one remembers that the propagation speed of transverse waves on, for example, a violin string, is $v_{bend} = (T/\mu)^{1/2}$, where T is the tension in the string. Our long filament behaves essentially as this violin string, and in the absence of any external forces the tension $T = 0$ and $v_{bend} = 0$.

Thermal fluctuations of interest

The thermal motion of the filament can be characterized by the methods outlined in Appendix B. We focus on a few representative measures of "disorder," mostly those that seem to be of general interest and for which experimental results are currently available.

Let us begin with statistics performed directly on quenched ensembles of thermally excited filaments, for example, the one shown in Fig. 2. It is convenient to compute the various deformations with respect to the axis of each filament. The definition of the axis coordinates for *bent* filaments is a nontrivial problem which requires some degree of arbitrariness (Egelman, 1986). We define the position of the axis near the ith monomer, $\mathbf{r}_i^0$, as

$$\mathbf{r}_i^0 = \frac{1}{13} \sum_{n=-6}^{n=6} \mathbf{r}_{i+n}, \tag{33}$$

where $\mathbf{r}_j$ is the location of the center of mass of monomer j. Because of the 13-monomer repeat of F-actin, the axis computed in this way is as smooth as that obtained from spline techniques, and we prefer it for its simplicity.

We must be careful with the contribution from the longest-wavelength modes, whose actual wavelengths cannot be determined without solving the finite filament problem with appropriate boundary conditions. We overcome this limitation by restricting the analysis to short segments of the filament. Within short lengths, the contribution of a long-wavelength mode may be treated as a nearly constant background. Also, the amount of data that can be extracted from a filament is larger for shorter segments, which is a welcome bonus.

Azimuthal angular disorder

To explore the azimuthal disorder we first compute $\mathbf{u}_i$, the unit vector connecting the center of mass of monomer i to its axis point: $\mathbf{u}_i = (\mathbf{r}_i - \mathbf{r}_i^0)/|\mathbf{r}_i - \mathbf{r}_i^0|$. The angle formed between monomers i ($i - 1$) and the axis is then $\psi_i - \psi_{i-1} = \arccos(\mathbf{u}_i \cdot \mathbf{u}_{i-1})$. In an unperturbed filament this angle is constant, $\Delta\psi = -166.15°$. We are interested in the fluctuations from equilibrium,

$$\delta_i \equiv \psi_i - \psi_{i-1} - \Delta\psi = \arccos(\mathbf{u}_i \cdot \mathbf{u}_{i-1}) - \Delta\psi. \quad (34)$$

Here δ_i is the angular disorder between consecutive monomers, as introduced by Egelman et al. (1982). The cumulative azimuthal, angular disorder after n monomers is then $\Delta_n = \sum_1^n \delta_m$, and

$$\langle \Delta_n^2 \rangle = \left\langle \left(\sum_{m=1}^{n} \delta_m \right)^2 \right\rangle = n\delta^2 + 2 \sum_{m=1}^{n-1} (n - m)\langle \delta_0 \delta_m \rangle, \quad (35)$$

where $\delta \equiv \langle \delta_i^2 \rangle^{1/2}$. If the δ_i are completely independent, then the correlations $\langle \delta_0 \delta_m \rangle$ are all zero, and the cumulative angular disorder grows as $\langle \Delta_n^2 \rangle = \delta^2 n$, as in the random cumulative disorder model of Egelman et al. (1982).

In Fig. 4 we plot $\langle \delta_0 \delta_m \rangle$ as a function of m. The correlations decay rapidly to zero, and successive correlations (for monomers m and $m + 1$) are strongly anticorrelated. On the other hand, the motions of monomers m and $m + 2$ (i.e., monomers within the same strand) are positively correlated. This indicates an opening and closing of the groove angle between the two long pitch strands. Such a motion could occur as a combination of the groove-angle swinging modes and torsional waves.The data in Fig. 4 are well fitted by the function $\langle \delta_0 \delta_m \rangle = \delta^2(-1)^m \exp(-0.012m - 0.082m^2)$, where $\delta = \langle \delta_i^2 \rangle^{1/2} = 5.23°$ is the rms of the angular disorder between any two consecutive monomers.

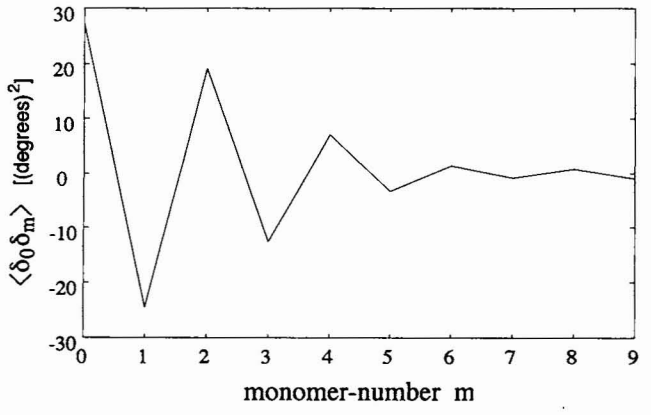

FIGURE 4 Correlations in the azimuthal angular disorder between monomers 0 and m, $\langle \delta_0 \delta_m \rangle$, as a function of the distance between monomers, m.

To estimate the cumulative angular disorder we now employ Eq. 35. For small m we use the data of Fig. 4, and for larger m, where the statistics from our ensemble cease to be accurate, we extrapolate from the analytical fitting function. The result is an angular disorder that accumulates asymptotically as $\langle \Delta_n^2 \rangle \sim \bar{\delta}_0^2 + \bar{\delta}^2 n$, with $\bar{\delta}_0 = 3.9°$ and $\bar{\delta} = 0.84°$. Thus, the overall effect is a *random* cumulative angular disorder, as in the Egelman–DeRosier model (Egelman and DeRosier, 1992). Notice, however, that the accumulation is much smaller than that deduced from EM. Whereas the azimuthal fluctuation of any individual monomer, δ, compares favorably with the EM measurements, the asymptotic $\bar{\delta}$ is substantially smaller, because of the anticorrelations of the opening and closing of the groove angle.

Fiber thickness

As a measure of the thickness of the fiber near the ith monomer, we propose the quantity

$$D_i = |(\mathbf{r}_{i+1} - \mathbf{r}_{i+1}^0) - (\mathbf{r}_i - \mathbf{r}_i^0)|. \quad (36)$$

Because the angle between $(\mathbf{r}_{i+1} - \mathbf{r}_{i+1}^0)$ and $(\mathbf{r}_i - \mathbf{r}_i^0)$ is approximately $\langle \psi \rangle = -166.15°$, close to 180° the difference between D_i and the actual thickness is a mere 3%. The fluctuations in the thickness are then given by

$$\Delta D = (\langle D_i^2 \rangle - \langle D_i \rangle^2)^{1/2}, \quad (37)$$

where the angle brackets denote an average over the index i and over all configurations. For the H model, we find $\Delta D = 0.48$ Å. We note that, because normal mode analyses are valid only in the harmonic regime of small oscillations, phenomena such as the formation of "bubbles" through disassociation of the two strands, as reported, for example by Bremer et al. (1991), are not predicted by this approach.

Bending and persistence length

The persistence length, λ, is a measure of the distance within which the filament is relatively rigid and the bending angle remains small. A straightforward computation of the persistence length would require the analysis of the radius of curvature of long segments of the filament. This requires, however, the specification of specific boundary conditions, as discussed earlier. An elegant way to overcome this requirement is to estimate the persistence length from the computed value of the coefficient of flexural rigidity; $\lambda = \xi/k_B T$. For the computation of ξ we simply use the dispersion relations (for an *infinite* filament) and Eq. 31, and hence our ignorance of the actual values of the long wavelengths is irrelevant (Eq. 31 is valid for all k near k_0). Using the value of $\xi = 4.3 \times 10^{-17}$ dyn cm^2, computed from the dispersion relations, we obtain $\lambda = 10$ μm.

Twisting within a strand

Twisting fluctuations *within* a strand should not be confused with twisting of the fiber as a whole, nor with the angular disorder discussed above. This fluctuation is a measure of the torsional flexibility of the *individual* strands. We define the twisting fluctuation within a strand as

$$\Delta\gamma_i = \gamma_i - \gamma_{i+2}, \tag{38}$$

where γ_i is the rotation angle of the ith monomer about its z axis. Because this fluctuation does not require the computation of the axis coordinates, it can be easily expressed in terms of thermal correlations. A detailed explanation of how this is done is given in Appendix B.

In Fig. 5 we plot the rms fluctuation in the strand twisting angle that is due to individual modes, $\langle\langle\Delta\gamma_\sigma(\phi)^2\rangle\rangle^{1/2}$, as well as the combined fluctuation of all modes with the same phase lag ϕ, $\langle\langle\Delta\gamma(\phi)^2\rangle\rangle^{1/2} = (\Sigma_\sigma\langle\langle\Delta\gamma_\sigma(\phi)^2\rangle\rangle)^{1/2}$, as computed from Eq. B9 (Appendix B) for the H model. Because $\Delta\gamma_\sigma(\phi)$ scales as $N^{-1/2}$, the rms fluctuation that is due to all modes is independent of the number of monomers, N. In fact, the results in Fig. 5 are multiplied by $N^{1/2}$ to be rendered N-independent (we have used $N = 100$ for the actual computation). We find $\langle\langle(\Delta\gamma)^2\rangle\rangle^{1/2} = 1.43°$ for the overall fluctuation that is due to all modes.

Comparison of results with different models

We now compare the results for the H model, the P model, the L model, and the T model of F-actin (see "F-actin models considered" in the Method section for a description of these models). For convenience, results are summarized in Table 1. Recall that the same potential energy form has been used in all cases (Eqs. 9–12). Differences arise solely as a consequence of the particular atomic interactions between monomers in each model. For example, the ratio of pairwise interactions along the longitudinal bond to that of the diagonal bond, N_{long}:N_{diag}, is a rough measure of the relative strength of the intramonomer bonds, and is strongly model-dependent.

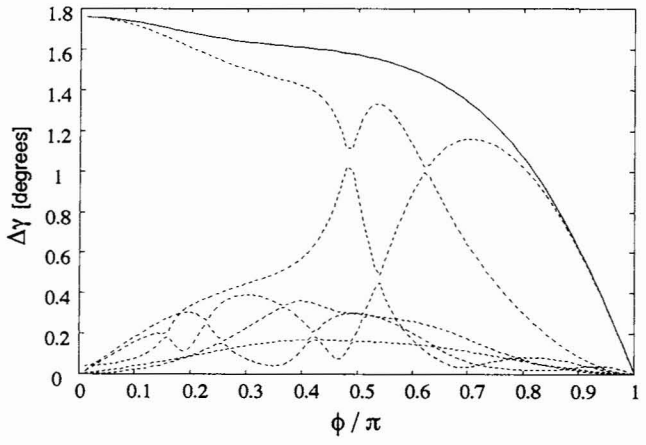

FIGURE 5 Twisting within a strand, $\Delta\gamma$, as a result of thermal excitations. The dashed curves represent the independent contributions of each of the six branches of modes (Fig. 3). The solid curve is the total contribution of all six branches, per a given wave-phase ϕ. The total thermal disorder in the twisting angle is obtained from the integral over this curve.

The H model of F-actin yields 301 diagonal and 856 longitudinal atomic interactions. The P model, identical to the H model except for a 13-residue loop (262–274), has a greater number of diagonal interactions (905) and almost the same number of longitudinal interactions (860), increasing the relative strength of the diagonal bond significantly. The L model, incorporating both a rebuilt "plug" as well as a rebuilt DNase I loop, has 1071 longitudinal and 596 diagonal interactions. The longitudinal interactions of subdomain 2 are strictly with the neighboring subdomain 3. The T model has the DNase I loop oriented in the cleft between subdomains 1 and 3 of the neighboring monomer in the long-pitch helix and has not rebuilt the 262–274 "plug". This results in a larger number (1366) of longitudinal interactions (subdomain 2 interacts with *both* subdomains 3 and 1 of the neighboring monomer) and a smaller number (205) of diagonal interactions.

The only fitting parameter in our theory, C, is computed separately for each model, so that the filament exhibits a stretching spring constant of $K = 43.9$ pN/nm (see "Computation of the potential strength C"). As a result, the speed of acoustic pressure waves (in vacuum), $v_{long} = 1310$ m/s, is the same for all models. The last column in Table 1 lists the dependencies on changes in the fitting parameter, C. It may be used to draw further valuable conclusions. For example, both v_{long} and v_{tors} vary as $C^{1/2}$: it follows that the ratio v_{tors}/v_{long}, which is a measure of the torsional flexibility of the filament relative to its resistance to stretching, is independent of C and is only model-dependent!

The combined Gibbs contact energy of the diagonal and longitudinal bonds (Eq. B4) are listed in Table 1. They are roughly the same for all models, ~18 kcal/mol. The Gibbs energies are very insensitive to changes in C. For example, doubling the value of C merely reduces ΔG from 18.4 to 17.2 kcal/mol (for the H model). By combining ΔG with the relative strength of the bonds, N_{long}:N_{diag}, one obtains estimates of the Gibbs energy for each of the intramonomer bonds:

$$\Delta G_{diag} = \frac{N_{diag}}{N_{long} + N_{diag}}\,\Delta G \tag{39}$$

(and likewise for ΔG_{long}). The values computed in this way are consistent with independent estimates of Erickson (1989) and K.C. Holmes (Max-Planck Institute for Medical Research, Heidelberg, 1994).

The next four rows in Table 1 pertain to flexibility constants of F-actin. The Young's modulus per inverse unit area, ES, was used to calibrate C and is therefore the same for all models. The coefficient of torsional rigidity, a measure of resistance to an external torque, changes little as a consequence of the (diagonal) "plug" orientation, as seen in the similar values of ζ for the H and P models. However, ζ increases significantly for both the T and L models, where there are increased numbers of

TABLE 1 Comparison of results for the various models

	H	*P*	*L*	*T*	C Dependence
N_{long}: N_{diag}	856:301	860:905	1071:596	1366:205	none
C (kcal/mol Å^2)	0.0149	0.0132	0.0136	0.0115	C
v_{long} (m/s)	1310	1310	1310	1310	$\sqrt{C}$
v_{tors} (m/s)	410	426	494	484	$\sqrt{C}$
ΔG (kcal/mol)	18.4	17.8	17.7	18.4	negligible
ES (10^{-8} N)	4.4	4.4	4.4	4.4	C
ζ (10^{-17} dyn cm^2)	2.6	2.8	3.7	3.6	C
ξ (10^{-17} dyn cm^2)	4.3	5.1	5.8	4.8	C
λ (μm)	10	12	14	12	C
δ	5.2°	4.8°	5.3°	6.0°	$1/\sqrt{C}$
ΔD (Å)	0.48	0.39	0.36	0.46	$1/\sqrt{C}$
$\Delta\gamma$	1.43°	1.31°	1.13°	1.35°	$1/\sqrt{C}$
ω_{max} (10^{12}/s^{-1})	0.66	0.76	0.82	0.76	$\sqrt{C}$
frequency gaps (10^{12}/s^{-1})	0.44–0.46 0.55–0.60	0.52–0.56 0.61–0.65	0.50–0.53	0.44–0.48	$\sqrt{C}$
Relative amplitude of axial slipping	1.51	1	1.02	2.29	none
Relative amplitude of groove-angle swinging	1.51	1	1.03	1.96	none

longitudinal contacts. The flexural rigidity, ξ, is smallest in the H model, and increases if either the "plug" (P model) or the DNase I binding loop (T model) is reoriented to increase the number of diagonal or longitudinal bonds, respectively. In case both diagonal *and* longitudinal interactions are increased, as in the L model, this constant is even larger.

The persistence length has been computed from the estimates of ξ, $\lambda = \xi/k_BT$, and ranges from 10 μm for the H model to 14 μm for the L model. The variation in λ compares favorably with the published range, from 6 to 20 μm (Yanagida and Oosawa, 1978; Yanagida et al., 1984; Orlova and Egelman, 1992, 1993). Notice that ES, ζ, ξ, and λ have the same dependence on the fitting parameter C, and hence the ratio of any two of these quantities is only model-dependent.

The next three rows in Table 1 report the magnitude of various thermal fluctuations. The first pertains to the azimuthal angular disorder, listing the rms disorder of an arbitrary monomer, $\delta = \langle\delta_i^2\rangle^{1/2}$. For all four models the angular disorder accumulates randomly, as proposed by Egelman et al. (1982), and the rms fluctuation of any given monomer is comparable with their estimates of δ. However, we find that the azimuthal fluctuations of successive monomers are highly anticorrelated, because of the opening and closing of the groove angle between the long-pitch helices, which is a dominant mode of motion. This results in an angular disorder accumulation that is significantly smaller than in the model of Egelman et al. Thus, while thermal fluctuations naturally give rise to random cumulative disorder, the magnitude of the cumulative disorder observed in EM is not explained by this analysis.

The variations in thickness, ΔD, are also measured on ensembles of thermally quenched filaments. Not surprisingly, the variation in radial thickness decreases as the number of diagonal contacts increase. The present values are much smaller than the variation in thickness reported in the literature (see, for example, Bremer et al., 1991). However, this is not surprising, as a normal mode analysis pertains only to small oscillations and hence does not model the effects of strand separation.

Finally, $\Delta\gamma$, corresponding to twisting of the monomers *within* a long-pitch helix, was computed by means of Eq. B9. The twisting within strands is largest for the H model and decreases as either the number of diagonal contacts (P model) or the number of longitudinal contacts (T model) increases. In case both types of contacts increase (L model), the twisting within a strand decreases further. Apparently, the diagonal contacts help to stabilize the long-pitch helix.

The last four rows report on variations in mobilities typical to actin, as a result of the different models. The maximal frequency of oscillation, ω_{max}, reflects how strongly adjacent monomers interact and is larger the stronger the interaction. The frequency gaps are also highly model-dependent. In the L and T models there is a single band, as opposed to two bands of inaccessible frequencies in the H and P models.

The axial slipping motion and the groove-angle swinging motion discussed earlier are maximal for the model with the least diagonal interaction, namely, the T model. Conversely, these motions are smallest when the number of diagonal contacts is maximal (P model). The reorientation of the 13 residues of the "plug," a mere 3% of the mass of the monomer, decreases both the axial slipping and the groove-angle-swinging motion by ~50%, as seen from a comparison of the H and P models. Strong longitudinal contacts in the absence of the strong diagonal contacts provided by the "plug" (T model) enhance these mobilities dramatically.

SUMMARY AND DISCUSSION

We have developed a normal mode algorithm to analyze the dynamical and mechanoelastic properties of the actin fila-

ment. The computation proceeds from first principles and does not rely on a generalized theory of elasticity of continuum media. This initial analysis, done in vacuo, computes the normal modes of the filament resulting from rigid-body translations and rotations of monomers: internal vibrational motions within monomers are not currently modeled. We assume that the published coordinates of F-actin are stable (minimum-energy) configurations and that all intermonomer interactions are mediated by nearest-neighbor atomic pairs. The bond strength of each noncovalent intermonomer interaction is parameterized by a harmonic potential using a single parameter to characterize the bond strength. This parameter is scaled to experimental results and is the only adjustable parameter in our analysis: agreement between predicted and published experimental results, therefore, cannot be ascribed to excessive parameter fitting.

Within the current formulation, the computed dispersion relation completely characterizes the kinetics, the elastic properties, and thermodynamic potentials of F-actin. We have computed the speeds of propagation of elementary waves; longitudinal pressure waves, torsional waves, and transverse bending waves, and their related elastic parameters; the Young's modulus, the coefficient of torsional rigidity, and the coefficient of flexural rigidity. These parameters permit predictions of deformations induced by external torques and forces exerted on F-actin. As recent experiments indicate that approximately 40–60% of sarcomere compliance resides in the thin filaments (Huxley et al., 1994; Wakabayashi et al., 1994; Goldman and Huxley, 1994), the derivation of the longitudinal, torsional, and bending stiffnesses of the actin filament permits quantitative comparisons to experimental results.

The computed eigenmodes describe a broad range of motions, which have correlation lengths that extend from neighboring monomers to the entire length of the filament. Isolated motions include relative oscillations of the two long-pitch strands, such as the "groove-swinging" motion involving azimuthal displacements of the strands. This motion alternately widens and narrows the groove angle between the two strands. We also observe an axial "slipping" motion of the long-pitch strands relative to each other, a motion that looks like a sawing-type movement in animations. There are further modes that pertain to slight *radial* extensions and contractions of the filament, as well as many other types of twisting and tilting mobilities between neighboring monomers.

The flexibility characteristics of the filament, as evidenced by the computed persistence length, elastic coefficients, and thermal fluctuations, are surprisingly sensitive to the particular F-actin model under consideration. For example, the reorientation of the 13 plug residues (262–274), a mere 3% of the mass of the monomer, significantly reduces both the amounts of axial slipping and groove-angle swinging, as well as the twisting within strands. Apparently, a stronger diagonal anchoring, as modeled by the rebuilt plug, stabilizes not only the interstrand mobilities but also the intrastrand (long-pitch) helices.

The T and L models of F-actin illustrate the varying effects of the orientation of the DNase I binding region (residues 38–52) in subdomain 2 to filament stability. In the L model this loop is folded back onto subdomain 2, where it makes longitudinal contacts only with subdomain 3 of the neighboring monomer. In the T model, this loop interacts with subdomain 3 *and* with subdomain 1 of the neighboring monomer in the long-pitch helix. This results in a greater number of longitudinal contacts, at a higher radius, than in the L model. The torsional rigidity of the two models is almost equal, in spite of the rebuilt 262–274 loop incorporated in the L model, whereas the L model is stiffer in terms of the flexural rigidity. Not surprisingly, the greater number of longitudinal contacts in the T model confer greater stability for relative axial slipping and groove-angle swinging motions.

Recent experiments indicate that subdomain 2 assumes different conformations as a result of the state of the nucleotide (ATP or ADP), the identity of the bound cation, and solvent conditions (Orlova and Egelman, 1992, 1993). Site-directed mutagenesis experiments indicate that the chemical composition, and presumably therefore the structure, of the plug confers temperature-sensitive stability to the filament (Chen et al., 1993). It is therefore interesting that our computations show that physical properties of the filament, such as its stiffness, are drastically affected by the orientation of the DNase I binding region in subdomain 2. Indeed, it is intriguing to consider the possibility that actin can self-regulate its rigidity in a manner analogous to bacterial membranes, which maintain constant fluidity by temperature-sensitive regulation of the saturation of the fatty acids chains in the phospholipid bilayer.

The current analysis does not consider the contributions of internal flexibilities within the monomers to the overall dynamical spectrum of the filament. We are currently generalizing our analysis to include internal degrees of freedom within monomers. The internal degrees of freedom may give rise to internal friction. It will be interesting to see what is the combined effect of the friction and of the increased elasticity introduced by the internal degrees of freedom. We also do not take into account the effect of the solvent. The solvent will have a dramatic effect on the time scales of the modes, and it is important to quantify these effects for the analysis of experiments involving time scales slower than 1 μs (for example, Thomas et al., 1979; Prochniewicz et al., 1994).Ideally, we would like to extend the work done for simplified models of DNA in solvent (Schurr et al., 1992, and references therein) to the F-actin models discussed here.

We thank Michael Lorenz and Ken Holmes for the F-actin coordinates and for useful discussions. We thank Ed Egelman for assistance in the

analysis of ensembles of quenched thermal disorder and David Thomas for useful comments and references. We also thank Richard Gillilan, of the Cornell Theory Center, for the preparation of video animations of the computed motions. Finally, we gratefully acknowledge and thank a referee whose careful reading of the manuscript strengthened the paper. This material is based upon work supported by the National Science Foundation under grant No. MCB-9316109.

APPENDIX A

Computation of H and F

In this appendix we derive analytic expressions for the elements of the matrices **h**, **d**, **f**, and **g** (which are the blocks of **H** and **F**), under the potential of Eqs. 9, 11, and 12. An inspection of the problem shows that all the elements of these matrices can be written as sums of terms that involve the expression $\partial \mathbf{r}_n/\partial q_{m\mu}$ ($\mathbf{r}_n$ represents the position of some atom in monomer n; the derivative is taken with respect to the μth degree of freedom of monomer m). We first observe that

$$\frac{\partial \mathbf{r}_n}{\partial \mathbf{q}_{m\mu}} = 0, \qquad n \neq m. \tag{A1}$$

That is, monomer n does not move, unless there is an update of its *own* coordinates, $q_{n\mu}$. The block structure of the **H** and **F** matrices is a result of Eq. A1.

The derivative $\partial \mathbf{r}_n/\partial q_{n,\nu}$ does not depend on n, if written in terms of the local coordinates of monomer n. On the other hand, because products of the kind $(\partial \mathbf{r}_n/\partial q_{n,\nu})$ $(\partial \mathbf{r}_m/\partial q_{m,\mu})$ will be required, we need to refer these quantities to a global system of coordinates (we can arbitrarily choose the axes of monomer 0, say). We then have

$$\frac{\partial \mathbf{r}_n}{\partial q_{n\nu}} = \mathbf{U}^n\left(\frac{\partial \mathbf{r}_0}{\partial q_{0\nu}}\right), \tag{A2}$$

where **U** is the matrix of rotation connecting subsequent monomers (Eq. 1).

Expressions for each of the six degrees of freedom are easily worked out. For the parallel translations, $(q_1, q_2, q_3) = (x, y, z)$, we have

$$\frac{\partial \mathbf{r}}{\partial x} = \mathbf{i}, \qquad \frac{\partial \mathbf{r}}{\partial y} = \mathbf{j}, \qquad \frac{\partial \mathbf{r}}{\partial z} = \mathbf{k}, \tag{A3}$$

where **i**, **j**, and **k** denote unit vectors in the direction of the x, y, and z axes of the monomer, respectively. For the rotational degrees of freedom, $(q_4, q_5, q_6) = (\alpha, \beta, \gamma)$, we obtain

$$\frac{\partial \mathbf{r}}{\partial \alpha} = u_z\mathbf{j} - u_y\mathbf{k}, \quad \frac{\partial \mathbf{r}}{\partial \beta} = u_x\mathbf{k} - u_z\mathbf{i}, \quad \frac{\partial \mathbf{r}}{\partial \gamma} = u_y\mathbf{i} - u_x\mathbf{j}, \tag{A4}$$

where $(u_x, u_y, u_z) = \mathbf{u} \equiv \mathbf{r} - \mathbf{r}_{CM}$ denotes the vector connecting the center of mass of the monomer to the atom in question. In Eqs. A3 and A4 we have dropped the subscript 0.

We are now ready to compute the various matrix elements. Starting with **H**, we first confirm its block structure, using Eqs. 7 and A1. We then compute the **h** elements, applying Eqs. A3 and A4. It is seen that the matrix **h** itself has a block structure:

$$\mathbf{h} = \begin{pmatrix} \mathbf{M} & \bigcirc \\ \bigcirc & \mathbf{I} \end{pmatrix}. \tag{A5}$$

Each of the blocks is a 3×3 matrix. **M** is a diagonal matrix with diagonal terms equal to the total mass of an actin monomer, $\bigcirc$ is a matrix of zeros, and **I** is the tensor of inertia of the monomer,

$$\begin{aligned} I_{11} &= h_{44} = \sum zm(u_y^2 + u_z^2), \\ I_{12} &= h_{45} = -\sum mu_xu_y, \cdots, \text{etc.} \end{aligned} \tag{A6}$$

(the sums run over all atoms of the monomer).

To compute the **F** matrix, we use the potential of Eqs. 9, 11, and 12 in Eq. 5. Applying the rules of Eq. A1 and A2, we immediately recognize the block structure of **F**. The matrix **f** is given by

$$f_{\nu\mu} = \frac{\partial^2 E_{0,1}}{\partial q_{0\nu}\partial q_{1\mu}} = -C\sum\left(\hat{\mathbf{r}}_{01}\cdot\frac{\partial \mathbf{r}_0}{\partial q_{0\nu}}\right)\left(\mathbf{r}_{01}\cdot\frac{\partial \mathbf{r}_1}{\partial q_{1\mu}}\right), \tag{A7}$$

where $\hat{\mathbf{r}}_{01}$ represents a unit vector connecting an interacting pair of an atom on monomer 0 and another on monomer 1, $\hat{\mathbf{r}}_{01} = (\mathbf{r}_0 - \mathbf{r}_1)/|\mathbf{r}_0 - \mathbf{r}_1|$, and the sum runs over all such interacting pairs. The computation of the **f** elements is then completed with help of Eqs. A2–A4.

The **g** matrix is obtained in exactly the same way, except that the subscript 1 in Eq. A7 is replaced by 2 (the interacting pairs are, of course, also different). Roughly, **f** and **g** pertain to the diagonal bond and to the longitudinal bond, respectively. Finally, the elements of the **d** matrix are given by

$$d_{\nu\mu} = \frac{\partial^2 E_{01}}{\partial q_{0\nu}\partial q_{0\mu}} + \frac{\partial^2 E_{01}}{\partial q_{1\nu}\partial q_{1\mu}} + \frac{\partial^2 E_{02}}{\partial q_{0\nu}\partial q_{0\mu}} + \frac{\partial^2 E_{02}}{\partial q_{2\nu}\partial q_{2\mu}} \tag{A8}$$

and

$$\frac{\partial^2 E_{nm}}{\partial q_{n\nu}\partial q_{n\mu}} = C\sum\left(\hat{\mathbf{r}}_{nm}\cdot\frac{\partial \mathbf{r}_n}{\partial q_{n\nu}}\right)\left(\hat{\mathbf{r}}_{nm}\cdot\frac{\partial \mathbf{r}_m}{\partial q_{n\mu}}\right). \tag{A9}$$

The different sums run over the interacting pairs of the relevant monomers. Notice that the matrix **F** is proportional to C, and hence the eigenfrequencies, ω, are proportional to $C^{1/2}$. This relation may be used to derive the dependence of our various results on the fitting parameter C (as, for example, in the last column of Table 1).

APPENDIX B

Thermodynamics of the filament

The normal modes and eigenfrequencies can be employed to compute various thermodynamic potentials, as well as to characterize the thermal motion of a fiber in a heat bath.

From Eqs. 4 and 18, and imposing the normalization condition of Eq. 19, we obtain the potential energy

$$\langle E_p\rangle = \frac{1}{2}\frac{N}{2}\sum_\phi\sum_\mu \alpha_\mu(\phi)^2\omega_\mu(\phi)^2, \tag{B1}$$

where $\langle\cdots\rangle$ denotes a temporal average. Because the normal modes behave like independent harmonic oscillators, we have from the statistical thermodynamics of such an ensemble (Landau and Lifshitz, 1958)

$$\langle E_p\rangle = \sum_\phi\sum_\mu \frac{\hbar}{2\omega_\mu(\phi)}\coth\left(\frac{\hbar\omega_\mu(\phi)}{2k_BT}\right). \tag{B2}$$

Comparing this with Eq. B1 yields the amplitudes $\alpha_u(\phi)$ that is due to thermal excitation at temperature T. For ω's small enough, one obtains the classical expression (Levitt et al., 1985)

$$\alpha_\mu(\phi) = (2k_BT/N\omega_\mu(\phi)^2)^{1/2}. \tag{B3}$$

The frequencies of F-actin are indeed within this classical range. Other thermodynamic potentials are given in terms of the eigenfrequencies, similar to Eq. B2. For example, the Gibbs free energy associated with the thermal vibrational motion of the fiber is given by (see, for example, Hill, 1960)

$$\Delta G = \sum_\phi\sum_\mu\left(\frac{\hbar\omega_\mu(\phi)}{2} + k_BT\ln(1 - e^{-\hbar\omega_\mu(\phi)/k_BT})\right). \tag{B4}$$

We can now compute time-averaged correlations between the motions of monomers j and $(j + n)$. Using Eq. 18, and the fact that $\langle \cos(\omega t + \delta)\cos(\omega' t + \delta')\rangle_t = (1/2)\delta_{\omega\omega'}$ we get

$$\langle q_{j\nu} q_{j+n,\mu}\rangle = \frac{1}{2}\sum_{\phi}\sum_{\sigma} \alpha_\sigma(\phi)^2 \,|\, A_{\nu\sigma}(\phi)A_{\mu\sigma}(\phi) \,|\, \cos(j\phi + \theta_{\nu\sigma}(\phi) + \delta'_\sigma(\phi)) \quad \text{(B5)}$$

$$\times \cos((j+n)\phi + \theta_{\mu\sigma}(\phi) + \delta'_\sigma(\phi)).$$

A second average can then be performed over random initial conditions, i.e., over the phases $\delta'_\sigma(\phi)$. This is also equivalent to averaging over the location of the first monomer, j. We obtain

$$\langle\langle q_{j\nu} q_{j+n,\mu}\rangle\rangle = \frac{1}{4}\sum_{\phi}\sum_{\sigma} \alpha_\sigma(\phi)^2 \,|\, A_{\nu\sigma}(\phi)A_{\mu\sigma}| \,\cos(n\phi + \theta_{\nu\sigma}(\phi) - \theta_{\mu\sigma}(\phi)), \quad \text{(B6)}$$

where the additional set of angle brackets denotes the spatial average. Notice the independence from j of the result. As a special case, we obtain the rms thermal fluctuation of the νth degree of freedom of a monomer:

$$\langle\langle q_{j\nu}^2\rangle\rangle = \frac{1}{4}\sum_{\phi}\sum_{\sigma} \alpha_\sigma(\phi)^2 \,|\, A_{\nu\sigma}(\phi) \,|^2. \quad \text{(B7)}$$

Again, the result is independent of the position of the monomer in the fiber.

This approach can be used to compute thermal fluctuations of interest. For example, consider the twisting within a strand, $\Delta\gamma_i$ (see "Twisting within a strand"). Using the double average notation, we express the fluctuation in $\Delta\gamma_i$ as (see Eq. 38)

$$\langle\langle(\Delta\gamma)^2\rangle\rangle = \langle\langle(\gamma_i - \gamma_{i+2})^2\rangle\rangle = 2(\langle\langle\gamma_0^2\rangle\rangle - \langle\langle\gamma_0\gamma_2\rangle\rangle), \quad \text{(B8)}$$

where we have used the fact that there is no i dependence, because of the spatial average. Now, from Eqs. B6 and B7, and from $\gamma_i = q_{i6}$ (Eq. 2), we obtain the final expression

$$\langle\langle(\Delta\gamma)^2\rangle\rangle = \frac{1}{2}\sum_{\phi}\sum_{\sigma} \alpha_\sigma(\phi)^2 \,|\, A_{6,\sigma}(\phi) \,|^2 (1 - \cos 2\phi) = \sum_{\phi}\sum_{\sigma} \langle\langle(\Delta\gamma_\sigma(\phi))^2\rangle\rangle. \quad \text{(B9)}$$

Here $\Delta\gamma_\sigma(\phi)$ is the fluctuation in the twisting angle that is due to the σ branch of the normal modes at phase lag ϕ. The final computation is possible from a knowledge of the eigenvalues and eigenvectors, with $\alpha_\sigma(\phi)$ given by Eq. B3.

REFERENCES

Bremer, A., R. C. Millonig, R. Sütterlin, A. Engel, T. D. Pollard, and U. Aebi. 1991. The structural basis for the intrinsic disorder of the actin filament: the "lateral slipping" model. *J. Cell Biol.* 115(3): 689–703.

Chen, X., R. K. Cook, and P. Rubinstein. 1993. Yeast actin with a mutant in the "hydrophobic plug" between subdomains 3 and 4 ($L_{266}D$) displays a cold-sensitive polymerization defect. *J. Cell Biol.* 123(5): 1185–1195.

Diamond, R. 1990. On the use of normal modes in thermal parameter refinement: theory and application to bovine pancreatic trypsin inhibitor. *Acta Crystaliog.* A46:425–435.

Doolittle, R. F. 1992. Reconstructing history with amino acid sequences. *Protein Sci.* 1:191–200.

Egelman, E. H., N. Francis, and D. J. DeRosier. 1982. F-actin is a helix with a random variable twist. *Nature (London)* 298:131–135.

Egelman, E. H. 1986. An algorithm for straightenning images of curved filamentous structures. *Ultramicroscopy* 19:367–374.

Egelman, E. H., and D. J. DeRosier. 1992. Image analysis shows that variations in actin crossover spacings are random, not compensatory. *Biophys. J.* 63:1299–1305.

Erickson, H. P. 1989. Co-operativity in protein-protein association. The structure and stability of the actin filament. *J. Mol. Biol.* 206: 465–474.

Faure, P., A. Micu, D. Perahia, J. Doucet, J. C. Smith, and J. P. Benoit. 1994. Correlated intramolecular motions and diffuse x-ray scattering in lysozyme. *Nature Struct. Biol.* 1:124–128.

Goldman, Y. E., and A. F. Huxley. 1994. Actin compliance: Are you pulling my chain? *Biophys. J.* 67:2131–2136.

Goldstein, H. 1980. *Classical Mechanics,* 2nd ed. Addison-Wesley Publishing Co., Reading Ma.

Hatta, I., H. Sugi, and Y. Tamura. 1988. Stiffness changes in frog skeletal muscle during contraction recorded using ultrasonic waves. *J. Physiol.* 403:193–209.

Hill, T. L. 1960. *An Introduction to Statistical Thermodynamics.* Addison-Wesley, Reading, MA.

Holmes, K. C., D. Popp, W. Gebhard, and W. Kabsch. 1990. Atomic model of the actin filament. *Nature (London)* 347:44–49.

Huxley, H. E., A. Stewart, H. Sosa, and T. Irving. 1994. X-ray diffraction measurements of the extensibility of actin and myosin filaments in contracting muscle. *Biophys. J.* 67:2411–2421.

Kabsch, W., H.-G. Mannherz, D. Suck, E. Pai, and K. C. Holmes. 1990. Atomic structure of the actin:DNase I complex. *Nature (London)* 347: 37–44.

Kidera, A. and N. Gō. 1992. Normal mode refinement: crystallographic refinement of protein dynamic structure. I. Theory and test by simulated diffraction data. *J. Mol. Biol.* 225:457–475.

Kojima, H., A. Ishijima, and T. Yanagida. 1994. Direct measurement of stiffness of single actin filaments with and without tropomyosin by an in vitro manipulation. *Proc. Natl. Acad. Sci. USA* 91:12962–12971.

Landau, L. D., and E. M. Lifshitz. 1958. *Statistical Physics.* Pergamon Press, London.

Landau, L. D., and E. M. Lifshitz. 1959. *Theory of Elasticity.* Pergamon Press, London.

Levitt, M., P. Stern, and C. Sander. 1985. Protein normal-mode dynamics: trypsin inhibitor, crambin, ribonuclease and lysozyme. *J. Mol. Biol.* 181: 423–447.

Lorenz, M., D. Popp, and K. C. Holmes. 1993. Refinement of the F-actin model against X-ray fiber diffraction data by the use of a directed mutation algorithm. *J. Mol. Biol.* 234:826–836.

Marion, J. B. 1970. *Classical Dynamics of Particles and Systems,* 2nd ed. Academic Press, New York.

McLaughlin, P. J., J. T. Gooch, H.-G. Mannherz, and A. G. Weeds. 1993. Structure of gelsolin segment 1-actin complex and the mechanism of filament severing. *Nature (London)* 364:685–692.

Miki, M., and T. Kouyama. 1994. Domain motion in actin observed by fluorescence resonance energy transfer. *Biochemistry* 33: 10171–10177.

Orlova, A., and E. H. Egelman. 1992. Structural basis for the destabilization of F-actin by phosphate release following ATP hydrolysis. *J. Mol. Biol.* 227:1043–1053.

Orlova, A., and E. H. Egelman. 1993. A conformational change in the actin subunit can change the flexibility of the actin filament. *J. Mol. Biol.* 232:334–341.

Popp, D., V. V. Lednev, and W. Jahn. 1987. Methods of preparing well-oriented sols of F-actin containing filaments suitable for x-ray diffraction. *J. Mol. Biol.* 181:423–447.

Prochniewicz, E., Q. Zhang, P. Janmey, and D. D. Thomas. 1994. Gelsolin: a new tool to study dynamics of actin. *Biophys. J.* 66(2):Tu-Pos317.

Schurr, J. M., B. S. Fujimoto, P. Wu, and L. Song. 1992. Fluorescence studies of nucleic acids: dynamics, rigidities, and structures. In *Topics in Fluorescence Spectroscopy*, Vol. 3: Biochemical Applications. J. R. Lakowicz, editor. Plenum Press, New York. 137–229.

Schutt, C. E., J. C. Myslik, M. D. Rozycki, N. C. W. Goonesekere, and U. Lindberg. 1994. The structure of crystalline profilin-β-actin. *Nature (London)* 365:810–816.

Sosa, H., D. Popp, G. Ouyang, and H. E. Huxley. 1994. Ultrastructure of skeletal muscle fibers studied by a plunge quick freezing method: myofilament lengths. *Biophys. J.* 67:283–292.

Thomas, D. D., J. C. Seidel, and J. Gergely. 1979. Rotational dynamics of spin-labeled F-actin in the sub-millisecond time range. *J. Mol. Biol.* 132: 257–273.

Tirion, M. M., and D. ben-Avraham. 1993. Normal mode analysis of G-actin. *J. Mol. Biol.* 230:186–195.

Tirion, M. M., D. ben-Avraham, M. Lorenz, and K. C. Holmes. 1995. Normal modes as refinement parameters for the F-actin model. *Biophysical J.* 68(1):5–12.

Wakabayashi, K., Y. Sugimoto, H. Tanaka, Y. Ueno, Y. Takezawa, and Y. Amemiya. 1994. X-ray diffraction evidence for the extensibility of actin and myosin filaments during muscle contraction. *Biophys. J.* 67:2422–2435.

Yanagida, T., and F. Oosawa. 1978. Polarized fluorescence from epsilon-ADP incorporated into F-Actin in a myosin S1 complex. *J. Mol. Biol.* 126:507–524.

Yanagida, T., M. Nakase, K. Nishiyama, and F. Oosawa. 1984. Direct observation of motion of single F-actin filaments in the presence of myosin. *Nature (London)* 307:58–60.